University of São Paulo
Institute of Astronomy, Geophysics and Atmospheric Sciences
Astronomy Department

Francisco Junqueira

Three-dimensional MHD simulation of starburst galaxies: targets for the Cherenkov Telescope Array and the ASTRI Mini Array

São Paulo
2022

Francisco Junqueira

Three-dimensional MHD simulation of starburst galaxies: targets for the Cherenkov Telescope Array and the ASTRI Mini Array

Graduation work presented at the Astronomy Department of the Institute of Astronomy, Geophysics and Atmospheric Sciences of the University of São Paulo as a partial requirement for the degree of Bachelor in Sciences.

Basic research in Astronomy

Advisor: Prof. Elisabete M. de Gouveia Dal Pino, PhD

São Paulo

2022

to my little girl, Isabela

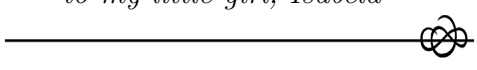

Acknowledgements

My first thank you goes to Professor Elisabete M. de Gouveia Dal Pino. Beyond her role as my academic advisor, which she did exceptionally, she served as a mentor, she was always there when I needed her support, reviewing my progress constantly. Words can't describe my admiration for her, academically and personally. Bete, thank you for the endless kindness and wisdom through this formative process.

To my friends from college (and for life), Raquel, Catarina, Stelinha, Giovani, Svetlana, and Luana: thank you for making the past 4 years much more enjoyable, there is love in SP and, for me, it is in our friendships. I would also like to extend my thanks to Professor Reinaldo Santos de Lima, for all the help and the valuable discussions we had along the road. I must thank Alessandra Lamastra, William Clavijo Bohórquez, and Claudio Melioli for their guidance and support on my research.

My deepest gratitude is to my family, thank you for all the support and love, my accomplishments were, primarily, because of you. I highlight my two truly exceptional brothers, Pedro and Lucca: you were fundamental for me to overcome the challenges I faced in the last 4 years. Pedro, thank you for being a very important part of my life since we were born, I am forever grateful for our friendship and for all the times it helped me to handle difficult situations. Lucca, in a way I can say these same words to you, but that being so, we need to move to the time of that "prazer, Ju"! A special thanks to my friend, Letícia, who was always there for discussions about anything that I was unsure on, the time you have invested in reading my countless drafts is unbelievably generous. To all of you: it would be inappropriate to articulate here how much I adore and depend on each of you.

Lastly, I would like to acknowledge the University of São Paulo and its Unified Scholarships Program (PUB-USP), and the São Paulo Research Foundation (FAPESP), for providing all the financial support and tools I needed.

This dissertation was written in LaTeX according to the IAGTESE template, for thesis and dissertations of the Institute of Astronomy, Geophysics and Atmospheric Sciences.

"*You're unlikely to discover something new without a lot of practice on old stuff [...]*"

Richard Feynmann

"*Consistency is the playground of dull minds.*"

Yuval Harari

Abstract

In this work, we present three-dimensional numerical magneto-hydrodynamic simulations of galaxies with intense activity of star formation, the so-called starburst galaxies, applied to the nearby starburst galaxy M82. The simulations were implemented in a modified version of the MHD code GODUNOV. We introduced an adiabatic wind driven mainly by Type II SNe (supernovae) randomly distributed (in space and time) in the galaxy center. M82 reveals a rich sample of stars in its central region (about 100 super star clusters within a radius $\sim$ 200 pc) computing a mass $\sim 2 \cdot 10^8\, M_\odot$, and SNe explode at a rate $\sim 0.1\,\mathrm{yr}^{-1}$ there; this starburst activity leads to the formation of a complex and highly fragmented environment, with cold and dense filaments immersed in a hot and less dense phase of the gas. We obtained that the interstellar medium, which was compressed and pushed away from the disk by the wind shock front, forms a high-pressure and hot shell wrapping a rarefied "bubble-like" structure with pressure $\sim 10^{-5}\,\mathrm{dyn/cm}^2$ that moves with a maximum vertical-velocity $\sim$ 190 km/s. We found, in a time interval of 450 kyr, the coexistence in the system of a warm to hot ($\leq 10^7$ K) and dense ($\sim 1 - 10\,\mathrm{cm}^{-3}$) filamentary structure, with a high temperature $\sim 10^7 - 10^8$ K and low density $\sim 0.1\,\mathrm{cm}^{-3}$ gas. Pressures $\sim 10^{-8} - 10^{-3}\,\mathrm{dyn/cm}^2$, which are up to eight orders of magnitude higher than the observed values for M82, were detected in the gas in the absence of the radiative cooling of its chemical species. Moreover, considering an adiabatic flow implied in gas phases with temperatures that are much hotter than the observations measurements. We also noticed that our choice of the plasma β parameter ($\beta = 300$) is large enough to make the initial magnetic field contribution dynamically not significant.

Resumo

Neste trabalho foram apresentadas simulações magneto-hidrodinâmicas tridimensionais de galáxias com surtos de formação estelar, com aplicação à galáxia de *starburst* M82. As simulações foram implementadas numa versão modificada do código MHD GODUNOV. Foi introduzido um vento adiabático impulsionado principalmente por supernovas de tipo II distribuídas arbitrariamente (no tempo e no espaço) no centro da galáxia. M82 exibe em sua região central um conjunto numeroso de estrelas (cerca de 100 super aglomerados estelares dentro de um raio de 200 pc) com massa total $\sim 2 \cdot 10^8\, M_\odot$, e explosões de supernovas a uma taxa de 1 evento a cada 10 anos; esta atividade de *starburst* induz a formação de um ambiente complexo e multi-fásico, com estruturas filamentares densas e frias imersas numa fase quente e rarefeita do gás. Verificou-se que o meio interestelar comprimido e arrastado pela frente de choque do vento cria uma zona quente e de alta pressão que envolve uma estrutura em forma de bolha com pressão $\sim 10^{-5}\,\mathrm{dyn/cm^2}$ que se afasta do disco a uma velocidade terminal ~ 190 km/s. As simulações resultaram num sistema em que, após 450 mil anos, filamentos com temperaturas $\leq 10^7$ K e densidades $\sim 1 - 10\,\mathrm{cm^{-3}}$ coexistem com uma fase mais quente $\sim 10^7 - 10^8$ K e tênue $\sim 0.1\,\mathrm{cm^{-3}}$ do gás. A ausência do resfriamento radiativo das espécies químicas presentes no gás permitiu que pressões $\sim 10^{-8} - 10^{-3}\,\mathrm{dyn/cm^2}$ se formassem na região central da galáxia, valores que são até oito ordens de magnitude maiores do que os medidos nas observações de M82. Além disso, considerar uma expansão adiabática implicou em fases do gás que são muito mais quentes do que o que é observado. Ademais, constatou-se que o campo magnético ajustado inicialmente não teve uma influência relevante nas características dinâmicas gerais do sistema, consequência da escolha $\beta = 300$, a qual representa uma forte predominância da pressão térmica sobre a pressão magnética no cômputo da pressão total do gás.

List of Figures

List of Tables

Contents

Chapter 1

Introduction

Starburst galaxies form stars at a rate of $\dot{M} \sim 10-100\,M_{\odot}\,\mathrm{yr}^{-1}$ (Gao e Solomon, 2004), which is one to two orders of magnitude higher than the star formation rate observed in ordinary galaxies just like the Milky Way. This rapid star formation leads to a correspondingly higher supernova (SN) rate of $\mathscr{R}_{SN} \sim 0.1 - 1\,\mathrm{yr}^{-1}$. Given the extreme efficiency of the supernova remnants in accelerating particles, we usually refer to starburst galaxies as cosmic rays (CRs) reservoirs.

In starburst galaxies, the combination of supernova explosions, stellar winds, and radiation pressure may drive galactic winds (GWs; see, e.g., Heckman et al. 1990), and these GWs conduct to the formation of a complex environment and a multi-phase interstellar medium (ISM; Ferrara et al. 1995). While traveling through the ISM, the CRs experience all of its phases, and hence undergo energy loss processes. Part of this non-thermal radiation is in the form of gamma rays.

The main goal of this project is to produce robust predictions of what we call "simulated data" of a given system, as the Cherenkov Telescope Array (CTA) will probably observe it, when operating. This same type of work was presented in the first half of 2022 as part of the student's graduation work. At that time, the analytical and simplified model discussed by Peretti et al. (2019, 2022) in relation to the gamma-ray emissivity of starburst galaxies (by both the starburst nucleus and the GW driven by the starburst activity) was employed as a template for the CTA Softwares - *ctools* (Knödlseder et al., 2016), and the instrument response functions (Cherenkov Telescope Array Consortium, 2019) - in order to generate synthetic gamma-ray spectra of three nearby starburst galaxies (M82, NGC253 & Arp220) which are already included in the CTA science core of its first 10 years of operation (Cherenkov Telescope Array Consortium, 2019).

At this time, our work focuses on studying the dynamical evolution of starburst galaxies by means of 3D MHD simulations, using the numerical codes and statistical tools already developed by our group, GAPAE (Portuguese acronym for *Grupo de Astrofísica de Plasmas e Altas Energias*), aiming to employ these numerical templates of star-forming regions to explore their association with the gamma-ray emission driven by CRs interacting with these systems. From the 3D MHD simulations we may obtain fiducial distributions of density, temperature, and magnetic fields in these systems.

The challenge of our work is to find out how to employ these "numerical starburst galaxies" as templates for the CTA Softwares. For that, we could investigate the effects of the CRs propagation in the ISM and in the GWs, by means of an effective pressure of the CRs on the plasma. We intend to add this effective pressure to the MHD equations and the equations of motion on the code, and hence take its effects into account in the simulations, and, finally, to compare the results with analytical studies (see, e.g., Everett e Zweibel 2011; Mao e Ostriker 2018). We then could combine the MHD simulations with a Monte Carlo description of the CRs propagation, in order to reproduce the radiative losses of the CRs by non-thermal processes (e.g., synchrotron, inverse Compton scattering, p-p and p-γ interactions) and to obtain the spectral energy distribution of these systems in the very high energies. This is a long tortuous task that was not included in the work here depicted, but will definitely be recaptured in forthcoming studies, in a similar way as it has already been performed in other studies of the group applied to other sources and environments.

Although we have studied the three starburst galaxies, M82, NGC253, and Arp220, in our last work, we are currently more interested in modeling suitable initial conditions for a M82-like galaxy, even though the approach here presented may be applied to other star-forming galaxies in general.

M82 is a starburst galaxy (Figure 1.1), located at about 3.9 Mpc away, with a disk of ~ 5 kpc radius and mass $\sim 10^{10}\, M_{\odot}$. Despite the fact that this galaxy has been classified as irregular, several observations (Mayya, Carrasco e Luna, 2005; Strickland e Heckman, 2009) revealed the presence of a bar and spiral arms. The striking galactic wind with filamentary structures (Figure 1.1) in M82 extends up to kilo-parsecs vertically away from the disk (Strickland and Heckman, 2009). Many studies suggest that this galaxy is in a persistent tidal interaction with the galaxy M81 over the last ~ 200 Myr, resulting in a

significant inflow of gas to the M82 core. The most important interaction has happened $\sim 2-5\cdot 10^8$ yr ago, causing a star formation burst of $\sim 10\,M_\odot\,\mathrm{yr}^{-1}$ that lasted ~ 50 Myr; two other starbursts must have occurred later (Barker, De Grijs e Cerviño, 2008). The starburst nucleus in the central region of M82 has a radius of ~ 500 pc, and the high star formation rate leads to a current supernova rate of $\sim 0.1\,\mathrm{yr}^{-1}$. The central region has a mass of $\sim 7\cdot 10^8\,M_\odot$, temperature $\sim 10^4-10^6$ K, densities $\sim 10^3-10^4\,\mathrm{cm}^{-3}$ and pressures $\geq 10^{-9}\,\mathrm{dyn/cm}^2$ (O'connell and Mangano, 1978). The SNe (supernovae) inject mass and energy at rates of $\sim 1\,M_\odot\,\mathrm{yr}^{-1}$ and $\sim 2\cdot 10^{42}\,\mathrm{erg/s}$, respectively (Strickland and Heckman, 2009).

Figure 1.1: Images from three of NASA's Great Observatories were combined to create this multiwavelength view of the starburst galaxy M82. Optical light from stars (yellow-green/Hubble Space Telescope) shows the disk. Another Hubble observation (orange) reveals a startlingly different picture of matter blasting out of the galaxy. The Spitzer Space Telescope infrared image (red) shows that cool gas and dust are also being ejected. Chandra's X-ray image (blue) reveals gas that has been heated to millions of degrees by the violent outflow. The eruption can be traced back to the central regions of the galaxy where stars are forming at a furious rate. Credit: X-ray: NASA/CXC/JHU/D.Strickland; Optical: NASA/ESA/STScI/AURA /The Hubble Heritage Team; IR: NASA/JPL-Caltech/Univ. of AZ/C. Engelbracht.

In regards to the two starburst galaxies left aside in the present work, i.e., NGC253 & Arp220:

Figure 1.2: ***Left***: The nearly edge-on spiral galaxy NGC253 is revealed here in an image from the Wide Field Imager (WFI) on the MPG/ESO 2.2-metre telescope at the La Silla Observatory. The image is based on data obtained through four different filters (R, V, H-α and OIII). Credit: ESO. ***Right***: The compound view shows a new ALMA Band 5 image of the colliding galaxy system Arp220 (in red) on top of an image from the NASA/ESA Hubble Space Telescope (blue/green). Credit: ALMA(ESO/NAOJ/NRAO)/NASA/ESA and The Hubble Heritage Team (STScI/AURA).

- **NGC253** (left side of Figure 1.2) is one of the weakest detected very high-energy gamma-ray sources (Abramowski et al., 2012; Abdalla et al., 2018) and is located at 3.5 Mpc away (Dalcanton et al., 2009). The star formation rate in the starburst nucleus can amount to $5\,M_{\odot}\,\mathrm{yr}^{-1}$ (Melo et al., 2002), leading to a rate of supernova explosions of $\mathscr{R}_{SN} \sim 0.03\,\mathrm{yr}^{-1}$ in the starburst region (Engelbracht et al., 1998). The molecular gas density in the central region of NGC253 is $580\,\mathrm{cm}^{-3}$ (Aharonian et al., 2005). Recent observations reveal an extended GW which is probably driven by the rapid star formation and the supernova explosions in the center of this galaxy (Sakamoto et al., 2011).

- **Arp220** (right side of Figure 1.2) is the closest Ultraluminous Infrared Galaxy (ULIRG) to Earth ($\sim$ 76.6 Mpc; e.g. Fleischhack and VERITAS Collaboration 2015). ULIRGs are mergers of galaxies, where much of the gas from the spiral disks fall into a common center of gravity. The merger creates an extreme molecular environment (> 1000 cm^{-3}) within a small region of a few hundred parsecs in size,

triggering a huge burst of star formation (Sanders e Mirabel, 1996). ULIRGs are relatively rare objects (Sanders e Mirabel, 1996), with Arp220 being the only ULIRG within 100 Mpc of Earth (Cherenkov Telescope Array Consortium, 2019). Arp220 has a star formation rate of $50-100\,M_{\odot}\,\mathrm{yr}^{-1}$, with a supernova explosion expected to occur every six months (Smith, Lonsdale e Lonsdale, 1998; Pavlidou e Fields, 2002). This supernova rate in Arp220 is the highest known in the local universe (Albert et al., 2007), making it the perfect object to study cosmic-rays production and their interaction with the ISM gas. The predicted gamma-ray emission of Arp220 is on the verge of current instruments. At TeV gamma-ray energies, CTA should detect Arp220 after a deep exposure, although its distance will limit the detection to a point-like source (Cherenkov Telescope Array Consortium, 2019).

In Chapter 2, we will summarize the results obtained during the first part of this project (TG I). In Chapter 3, we will outline our model with initial conditions for the starburst galaxy M82 and the results obtained from the numerical 3D MHD simulations, highlighting the formation of the multi-phase environment with filamentary structures which is observed in this galaxy, we will also briefly discuss whether our results are comparable or not to previous studies in this regard. And finally, in Chapter 4 we will draw our conclusions and present the perspectives for forthcoming works.

Chapter 2

Prospects for CTA observations of starburst galaxies

Contributors: A. Lamastra, E. Peretti, G. Morlino

As described in the previous TG I work, we generated synthetic gamma-ray spectra for the three nearby starburst galaxies M82, NGC253 & Arp220, assuming that their characteristics in the very high energies are well described by the model discussed in Peretti et al. (2019, 2022), in order to produce predictions of what CTA will probably observe from these objects, when operating.

2.1 Set-up

We performed our simulations using the analysis package ctools v.1.7.2, and the public CTA instrument response functions (IRF, v. prod5-v0). The sources are located at the galactic coordinates $\Theta = (\mathrm{RA}, \mathrm{Dec})$: $\Theta_{\mathrm{M82}} = (148.969\,\mathrm{deg}, 69.679\,\mathrm{deg})$ and $\Theta_{\mathrm{Arp220}} = (233.739\,\mathrm{deg}, 23.503\,\mathrm{deg})$, both are visible from the CTA Northern site; and $\Theta_{\mathrm{NGC253}} = (11.886\,\mathrm{deg}, -25.354\,\mathrm{deg})$, so it is visible from the CTA Southern site. M82 and Arp220 are both visible at a zenith angle $z < 50$ deg from the North, and NGC253 is visible at $z < 40$ deg from the South. We, therefore, chose the *North_z40_50h* and *South_z40_50h* IRFs.

We considered three spatial configurations for the galaxies: the point-like model, which is simply a source located at the galaxy coordinates; the extended model, a spherically symmetric source of radius 50 kpc centered at the position of the galaxy; and the composite configuration, that is the sum of a point-like source and an extended - this assumes it is possible to disentangle different gamma-ray emission regions (the starburst nucleus and the GW) in the galaxy. M82 and NGC253, located at about 3.9 Mpc and 3.5 Mpc, respectively,

Table 2.1 - Details of ctools simulations.

Source	IRF	Spatial Model	Exposure (h)
M82	*North_z40_50h*	Point-like	50
		Extended	100
		Composite	50
NGC253	*South_z40_50h*	Point-like	50
		Extended	100
		Composite	50
Arp220	*North_z40_50h*	Point-like	100

were covered by all spatial models; Arp220, at astonishing 77 Mpc away, was fixed to a point-like object (see Table 2.1). It is worth mentioning that CTA will be a pioneer in resolving extended sources in the gamma-ray band.

Three classes of telescope types are required to cover the full CTA energy range (20 GeV to 300 TeV). For its core energy range (100 GeV to 10 TeV), CTA is planning medium-sized telescopes (MSTs). The large-sized telescopes (LSTs) are planned to cover the unique low energy sensitivity of CTA between 20 and 150 GeV. The small-sized telescopes (SSTs) are sensitive to the highest energy gamma rays (between a few TeV and 300 TeV). The SSTs wide coverage and high sensitivity improve CTA chances of detecting the highest energy gamma rays. The CTA Southern site baseline array is located at the European Southern Observatory in the Atacama Desert (Chile), and is planned to be composed of 14 MSTs and 40 SSTs, while in the Northern site, located at the Observatorio del Roque de los Muchachos on the island of La Palma (Spain), 4 LSTs and 9 MSTs are planned to be installed. Consequently, the sensitivity of the Southern CTA site is dominant over its Northern site at the highest energies.

We considered a set of 10 energy bins covering the energy range from 0.1 to 100 TeV. The exposure times considered for each source and model are reported in Table 2.1.

2.2 Results

Figures 2.1 (M82), 2.2 (NGC253) and 2.3 (Arp220) show the spectra obtained with the simulations. For each model, we report the input spectrum (smooth black line) and the reconstructed spectrum in bins of energy. These simulations imply that considering from 50 to 100 hours of observations, CTA can be effectively used to constrain the maximum

energy (which is related to the high-energy cut-off of the spectrum) of the CRs accelerated in the starburst nucleus and in the starburst GWs, and the spectral slope for all the three galaxies in case they are point-like sources (Figures 2.1A, 2.2A, 2.3).

Considering an exposure $\geq$ 100 hours with CTA, M82 and NGC253 (less significantly: most energy bins are upper limits) are detectable as extended sources - see Figures 2.1B, 2.2B. It is quite surprising that the reconstructed high-energy spectrum of the extended NGC253 is not as good as the one of M82, since the last is visible from CTA northern array (where the sensitivity is somewhat worse than in the south). It may be related to the slightly higher gamma-ray flux of M82 over NGC253.

The inconsistency between the reconstructed spectra and the theoretical spectral energy distribution we take for granted indicates that the composite configuration for the two close-by starburst galaxies, M82 and NGC253, seems to be not reasonable in both cases (in regards to CTA angular resolution), given the model we assumed *a priori* for these galaxies in the high energies (Peretti et al., 2019, 2022), and the set-up of our simulations.

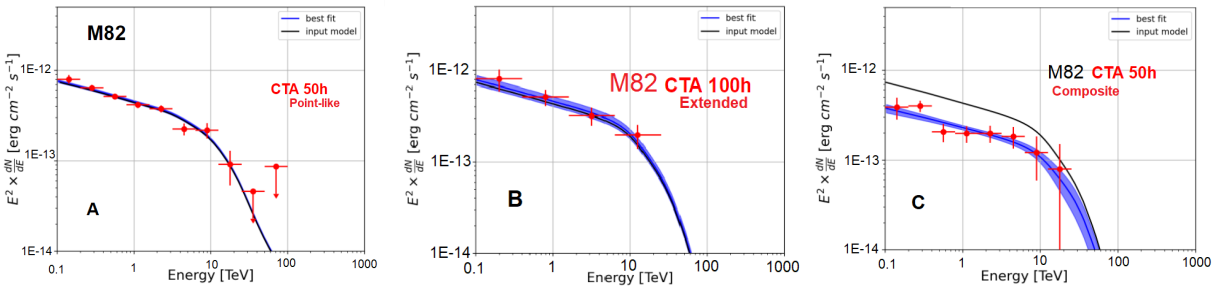

Figure 2.1: Reconstructed spectra for M82. **A**: point-like model and an exposure time of 50 hours; **B**: extended source observed for 100 hours; **C**: composite configuration, 50 hours of observation. This galaxy is visible from CTA northern site. In the diagrams, the smooth and black line represents the input spectrum, and the red points are the simulated bins of energy.

The results depicted above were obtained considering the analytical and simplified model presented by Peretti et al. (2019, 2022) as the theoretical parallel for the real gamma-ray emission of the three starburst galaxies M82, NGC253 & Arp220. However, a such simple description may not be the most ideal one, and the previous conclusions would be questionable accordingly. This is an issue we aim to solve by means of numerical MHD simulations that can give rise to a much more realistic illustration of those systems, perhaps even more encouraging prospects for the CTA observations of star-forming regions.

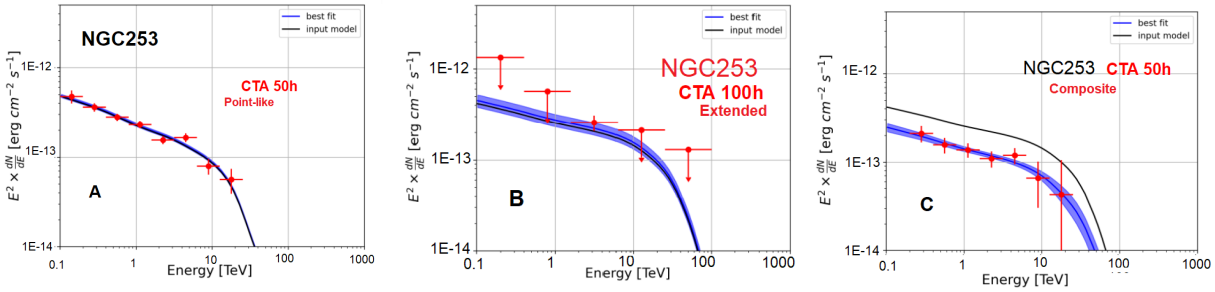

Figure 2.2: Reconstructed spectra for NGC253. **A**: considering a point-like model for the source and an exposure time of 50 hours; **B**: extended source observed for 100 hours; **C**: composite object, 50 hours of observation. This galaxy is visible from CTA southern array. In the diagrams, the smooth and black line represents the input spectrum, and the red points are the simulated bins of energy.

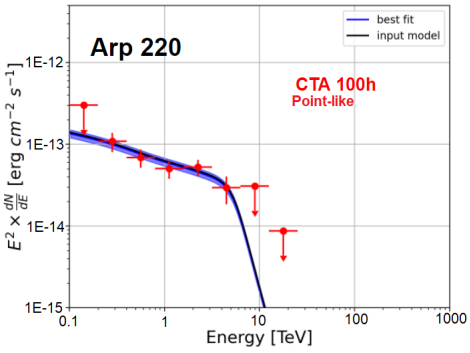

Figure 2.3: Reconstructed spectrum for Arp220, considering an exposure of 100 hours with CTA northern site. In the diagram, the smooth and black line represents the input spectrum, and the red points are the simulated bins of energy.

2.3 *Constraints on spectral parameters*

Since the point-like description provided the best results for all three galaxies (M82, NGC253 & Arp220), we used the reconstructed spectra to probe whether our simulations constrain or not the spectral parameters of the systems. The model discussed in Peretti et al. (2019) focused on the hadronic gamma-ray emission and hence we analyze the constraints on the spectral index and maximum energy of the power-law shaped spectrum of the accelerated CR protons. We also investigate the constraints on the influence of the SB galactic wind on the gamma-ray emission in M82 & NGC253, which is assumed to be described by Peretti et al. (2022).

The figures presented below show observations of the galaxies M82, NGC253 & Arp220 in the high energies by Fermi, HESS, and VERITAS, and the prospects for CTA observations of these galaxies in an energy range from 0.1 TeV up to 100 TeV. CTA observations

of Arp220 would be the first detection of an ULIRG in the very high energies band.

2.3.1 M82

The reconstructed gamma-ray spectral energy distribution (SED) for the point-like M82 in the high energies (Figure 2.1A) could be used to constrain the CR protons spectral index to some value between 2.25 and 2.3 (Figure 2.4A) and the maximum energy of the accelerated protons to a value higher than 500 TeV up to 100 PeV (Figure 2.4B). Figure 2.4B shows that CTA would also allow testing the effects of the internal gamma-ray absorption (inside the starburst nucleus) on the shape of the high energy spectrum.

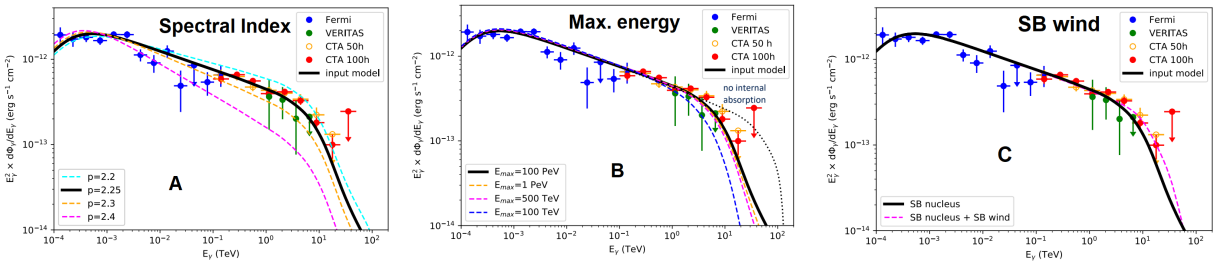

Figure 2.4: M82, point-like. Constraints on the **A**) spectral index and **B**) the maximum energy of the power-law spectrum of the accelerated CR protons, and on **C**) whether the SB galactic wind is relevant for the very high energy gamma-ray emission.

2.3.2 NGC253

The predictions for the CTA observations of a point-like NGC253 suggest that the CR protons spectral index is $\sim$ 2.3 and that their maximum energy should be higher than 500 TeV (see Figures 2.5A and 2.5B, respectively), as in M82. According to Figure 2.5C, constraints on the NGC253 SB galactic wind require an observation time of 100h, and also that it may be not as impressive as in M82 for the gamma-ray emission.

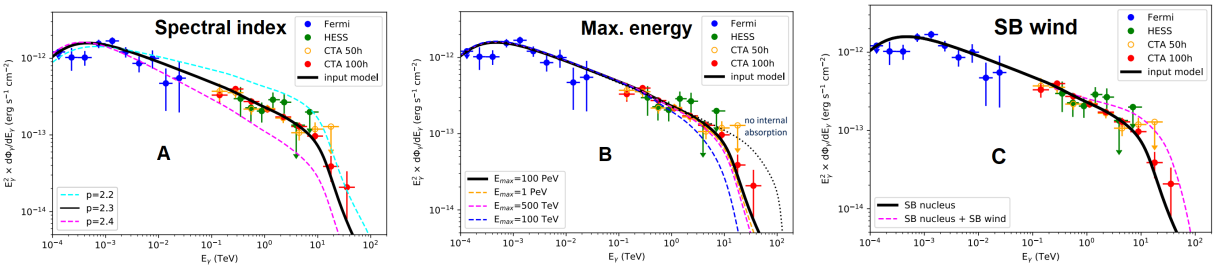

Figure 2.5: NGC253, point-like. Constraints on the **A**) spectral index and **B**) the maximum energy of the power-law spectrum of the accelerated CR protons, and on **C**) whether the SB galactic wind is relevant for the very high energy gamma-ray emission.

2.3.3 *Arp220*

Our simulations allow us to constrain the proton spectral index to 2.3 in Arp220 (Figure 2.6A), however, could not be used to constrain the proton maximum energy if it is higher than 100 TeV (Figure 2.6B).

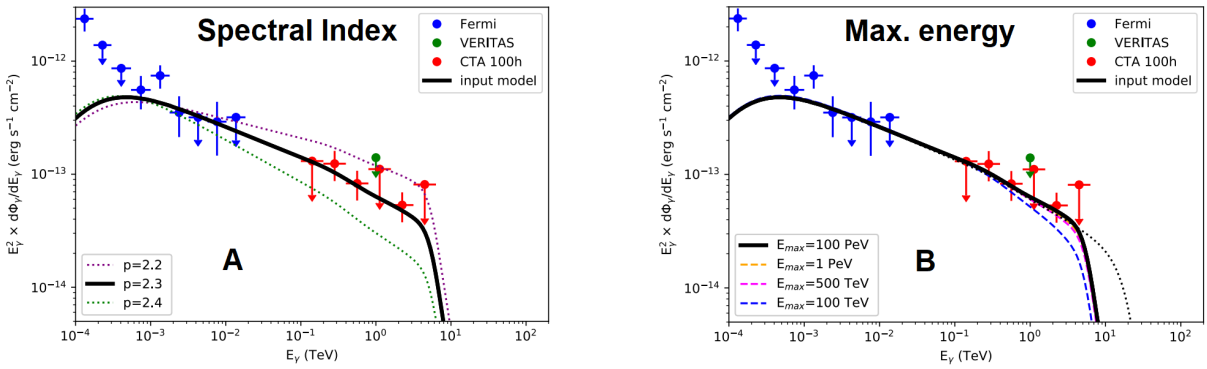

Figure 2.6: Arp220, point-like. Constraints on the **A**) spectral index and **B**) the maximum energy of the power-law spectrum of the accelerated CR protons.

Chapter 3

3D Numerical MHD Simulations of M82

3.1 Initial conditions for the simulations

In this part of the work, we consider a similar setup as employed in Geraissate (2010) and Melioli, de Gouveia Dal Pino e Geraissate (2013). In these works, the authors performed 3D hydrodynamic (HD) radiative cooling simulations of the M82 galaxy employing the YGUAZU code (Raga et al., 2002). Here, we consider the same system, but explore the effects of magnetic fields, by performing 3D magneto-hydrodynamic (MHD) simulations. Moreover, in this first study, we adopt for simplicity an adiabatic flow.

In the model we consider for the mass distribution of the gas in the galaxy, it is assumed that the gas is initially in rotational equilibrium in the gravitational potential of the galaxy. The total gravitational potential of the galaxy is due to the disk and the central stellar spheroid (we do not account for a dark matter halo because in such small scales around the galactic center it would be irrelevant, e.g. Strickland and Stevens 2000). Besides that, we assume an initial azimuthal symmetry in order to guarantee a dependency only on the cylindrical coordinates r and z.

The gravitational potential of the stars, $\Phi_{star}(r, z)$, is generated by a stellar distribution with a spheroidal King profile (e.g. Melioli et al. 2013)

$$\rho_*(r, z) = \frac{\rho_{*,0}}{[1 + (\omega/\omega_0)^2]^{3/2}}\,, \tag{3.1}$$

where $\rho_{*,0}$ is the density of stars within a radius $\omega_0 = 350$ pc, and $\omega^2 = r^2 + z^2$. The gravitational potential then takes the form

$$\Phi_{star}(r,z) = -\frac{GM_{star}}{\omega_0} \cdot \left[\frac{ln\Big\{(\omega/\omega_0) + \sqrt{1+(\omega/\omega_0)^2}\Big\}}{\omega/\omega_0} \right] , \tag{3.2}$$

where $M_{star} = 2 \cdot 10^8\ M_\odot$ is the stellar mass within the radius ω_0. To fix the singularity of Φ_{star}, we use

$$\lim_{\omega \to 0} \frac{ln\Big\{(\omega/\omega_0) + \sqrt{1+(\omega/\omega_0)^2}\Big\}}{\omega/\omega_0} = 1 ,$$

and set the stellar gravitational potential at the center of the spheroid to $\Phi_{star}(0,0) = -GM_{star}/\omega_0$.

The gravitational potential of the disk is assumed to be as given by Miyamoto and Nagai (1975):

$$\Phi_{disk}(r,z) = -\frac{GM_{disk}}{\sqrt{r^2 + \left(a + \sqrt{z^2+b^2}\right)^2}} , \tag{3.3}$$

where $a = 222$ pc and $b = 75$ pc are the radial and vertical scales of the disk, respectively, $M_{disk} = 2 \cdot 10^9\ M_\odot$ is the mass of the disk. The total gravitational potential of the galaxy is $\Phi_{tot}(r,z) = \Phi_{star}(r,z) + \Phi_{disk}(r,z)$.

In the steady state, the equation of motion of an ideal fluid is

$$(\mathbf{v} \cdot \nabla)\, \mathbf{v} = -\frac{1}{\rho} \nabla P - \nabla \Phi_{tot} , \tag{3.4}$$

and considering a circular flow with a velocity field $\mathbf{v} = v_\phi(r,z)\hat{\phi}$, we may rewrite Equation 3.4 in the form

$$-\frac{v_\phi^2}{r} = -\frac{1}{\rho}\frac{\partial P}{\partial r} - \frac{\partial \Phi_{tot}}{\partial r} . \tag{3.5}$$

In the plane $z = 0$ we can assume that the gas is predominantly supported by its rotation, then the solution of the equation of motion in the ϕ direction at $z = 0$ is simply given by

$$v_\phi^2(r,0) = e_{rot} \cdot \left(\frac{r \partial \Phi_{tot}}{\partial r} \right) , \tag{3.6}$$

where e_{rot} was introduced in order to account for other contributions to the rotational support of the gas (e.g., turbulence and thermal pressure as Eq. 3.5). In the case of a

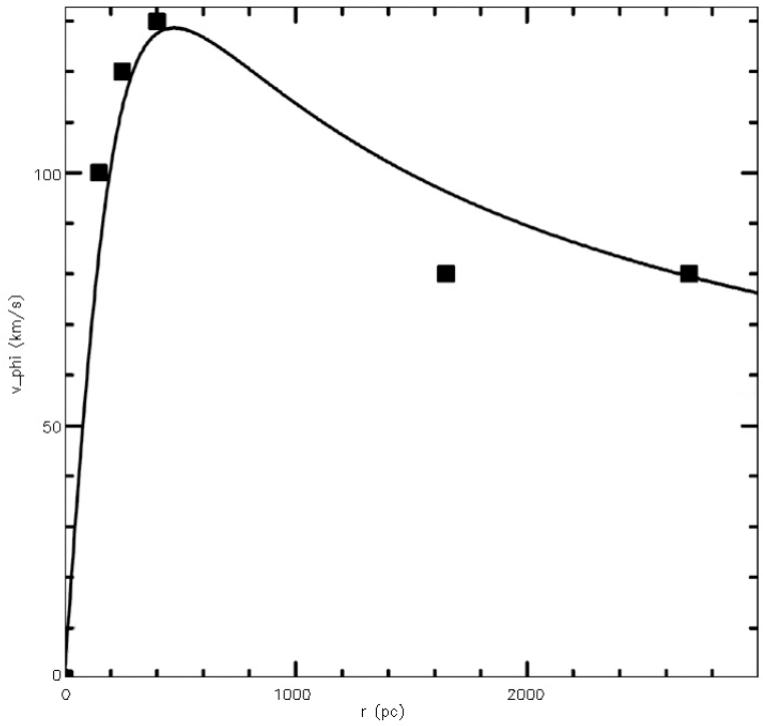

Figure 3.1: Initial rotation curve at $z = 0$ adopted for M82. The squares correspond to the observations of the galaxy, provided by Strickland and Stevens (2000).

gas supported **only** by its rotation, we should set $e_{rot} = 1$; in our model, $e_{rot} = 0.95$. The values of the velocity obtained in this way mimic quite well the rotation curve of a spiral galaxy (Melioli e de Gouveia Dal Pino, 2015): Figure 3.1 shows the initial rotation curve at $z = 0$ compared to the observations of M82 (Strickland and Stevens, 2000). In pursuance of reducing the rotational velocity above the plane and allowing for a non-rotating galactic halo, we assume, for simplicity, that the rotational velocity through space drops exponentially with

$$e = e_{rot} \cdot exp(-z/z_{rot})\,. \tag{3.7}$$

We shall set apart from the total gravitational potential Φ_{tot} the rotational effects, thereby we obtain an effective potential Φ_{eff}. The initial density profile of the gas is derived by setting a hydrostatic equilibrium and using the continuity equation to solve for the equation of motion (Equation 3.4) in terms of Φ_{eff} in the three directions (r, z and ϕ). These assumptions lead to the densities of the disk and the galactic halo (we are considering that the galaxy is the sum of these two components):

$$\rho_{disk}(r,z) = \rho_{disk,0} \cdot exp\left[-\frac{\Phi(r,z) - e^2 \cdot \Phi(r,0) - (1-e^2) \cdot \Phi(0,0)}{\left(1+\frac{1}{\beta}\right)(c^T_{s,disk})^2} \right], \tag{3.8}$$

$$\rho_{halo}(r,z) = \rho_{halo,0} \cdot exp\left[-\frac{\Phi(r,z) - e^2 \cdot \Phi(r,0) - (1-e^2) \cdot \Phi(0,0)}{\left(1+\frac{1}{\beta}\right)(c^T_{s,halo})^2} \right], \tag{3.9}$$

where $c^T_{s,disk}$ and $c^T_{s,halo}$ are the initial isothermal sound speeds in the disk and in the halo, respectively; $\rho_{disk,0}$ and $\rho_{halo,0}$ are the initial densities of each component. The term $(1+1/\beta)$ represents a correction due to the presence of an initially horizontal magnetic field in the system. It introduces extra support against gravity due to the magnetic pressure gradient that in the symmetry of this system simply adds to the thermal pressure gradient. The β parameter is defined as the ratio between the thermal pressure p and the magnetic pressure, i.e., $\beta = 8\pi p/B^2$.

The total density of the system is, therefore

$$\rho(r,z) = \rho_{disk}(r,z) + \rho_{halo}(r,z)\,, \tag{3.10}$$

and given that the density ρ is related to the thermal pressure through $p = \rho c_s^2$, we may write

$$p(r,z) = \left[\, \rho_{disk}(r,z) \cdot (c^T_{s,disk})^2 + \rho_{halo}(r,z) \cdot (c^T_{s,halo})^2 \,\right] / \gamma\,, \tag{3.11}$$

where γ is the adiabatic index (we adopted $\gamma = 5/3$).

In our model, the disk density is replaced by the halo density wherever the halo pressure is larger than the pressure of the disk, and vice versa. It avoids one phase to overlap the other within a single cell of the simulated box.

We adopt a disk temperature of $T_{disk} = 6.7 \cdot 10^4$ K and a halo temperature of $T_{halo} = 6.7 \cdot 10^6$ K, which correspond to $c^T_{s,disk} = \sqrt{\frac{k_B T_{disk}}{\mu\, m_p}} \sim 30 \cdot 10^5$ cm/s and $c^T_{s,halo} = \sqrt{\frac{k_B T_{halo}}{\mu\, m_p}} \sim 300 \cdot 10^5$ cm/s. We assume the gas to be dominated by hydrogen nuclei (protons, $m_p = 1.67 \cdot 10^{-27}$ kg), the factor μ is the mean molecular weight included because of the presence of much less abundant elements (such as helium); in the ISM, $\mu \sim 0.6$. Table 3.1 summarizes the parameters of the system, and Figure 3.2 shows the initial density and temperature distributions above the disk.

Table 3.1 - Initial conditions for a M82-like galaxy.

M_{star} $M_\odot$	M_{disk} $M_\odot$	ω_0 pc	a pc	b pc	$c^T_{s,disk}$ 10^5 cm/s	$c^T_{s,halo}$ 10^5 cm/s	e_{rot}	z_{rot} kpc	$\rho_{disk,0}$ cm^{-3}	$\rho_{halo,0}$ cm^{-3}	β
$2 \cdot 10^8$	$2 \cdot 10^9$	350	222	75	30	300	0.95	5	20	$2 \cdot 10^{-3}$	300

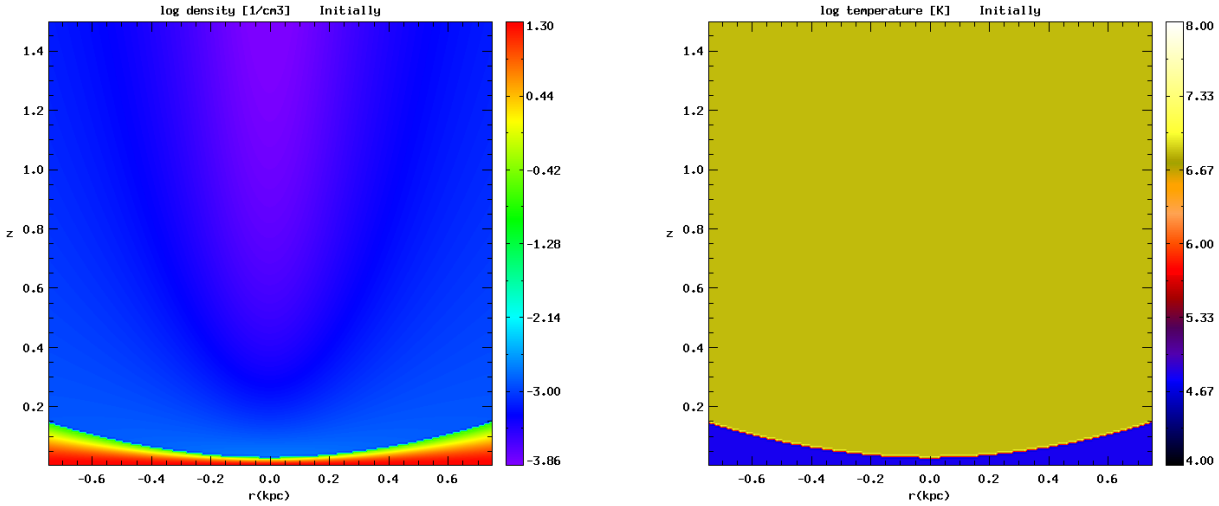

Figure 3.2: Edge-on view of initial logarithmic density (*left*) and temperature (*right*) distributions of the system (with density given in cm^{-3} and temperature in Kelvin). Distances are given in kpc.

We chose a high value of β-parameter (i.e., $\beta = 300$), which ensures a multi-phase ISM within the simulated box, since the stratification scale of the gas is $\propto (1 + \beta^{-1})$. We also set an initial horizontal and uniform magnetic field $B = 0.76\,\mu$G (microgauss) in the x-direction. We note that this value of β is large enough to make the initial magnetic field contribution dynamically not important.

The adopted box has physical dimensions of $1.5 \times 1.5 \times 1.5$ kpc in the x, y and z directions, respectively, and is covered by 256^3 cells (resolution of 5.8 pc per cell). We consider open boundaries, that is, the gas can escape through the boundaries of the computational domain.

3.2 Energy injection

It was assumed that the energy injected in the central region of the galaxy comes from SN types I and II. Although there are many other ways of injecting energy into the system (e.g., stellar winds and protostellar jets, and the super-massive black holes - SMBHs - in the galaxy center), the mean energy injected by protostellar jets is much smaller than

the energy injected by SN explosions (Mac Low e Klessen, 2004), while the wind, despite being non-negligible, last only a few years in the early life of stars (Melioli e de Gouveia Dal Pino, 2015); we do not consider a jet produced by an active central SMBH, therefore its contribution to the energy injection was ignored. The cosmic rays accelerated in the SN shock fronts and in the stellar winds generate considerable pressure in the ISM, inject energy and play an important role in the star formation processes and may drive GWs (Semenov, Kravtsov e Caprioli, 2021), however in the present work we do not take their effects into account.

In this work, we study the evolution of the initial system up to 450 kyr, a relatively short time range compared to the time scale of Type I SNe from less massive stars (which live much longer than the more massive stars that in turn explode as Type II SNe). For this reason, in this study we assume a very low SNI rate of 0.2 explosion each century. Each SNI explosion is associated with a random position in the stellar bulge of the galaxy at a random time between 0 and t_s, where t_s represents how long the stellar activity lasts. The positions are randomly generated and weighted by the stellar density profile within the bulge (Eq. 3.1), that is, the higher the density of stars, the higher the probability of a SNI taking place in that region.

To introduce the Type II SNe we assume a cylindrical starburst nucleus in the central region of the galaxy, with a radius of 300 pc and a height of 160 pc above and below the disk. Considering a SNII rate of $0.1\,\mathrm{yr}^{-1}$, we expect to have $4.5 \cdot 10^4$ SNe in a time interval of 450 kyr. As for the SNI, each SNII is associated with a random position (r, z), where $0 < r < 300$ pc and $-160 < z < 160$ pc, and a time between 0 and t_s.

Each SN (both type I and type II) injects an average luminosity of $6 \cdot 10^{41}\,\mathrm{erg\ s}^{-1}$ and a mass of $16\,M_\odot$ (for the SNII) or $1\,M_\odot$ (for the SNI). A single SNII (SNI) explosion injects energy and mass in a time interval of 30 yr (2000 yr). We adopt a SN heating efficiency of 100% (Melioli e de Gouveia Dal Pino, 2004), which implies that all the energy released by a SN explosion is injected (in a single cell) in the form of thermal energy into the ISM.

Although we produce one output each 75 kyr until 450 kyr, in our model we consider that the stellar activity could last for 10 Myr, since in later stages of this study we intend to investigate the effects of the radiative (atomic and molecular) cooling and the consequent development of a highly complex and multi-phase environment after a few Myr.

The energy injection of each SN is distributed according to a spherical gaussian weight

function:

$$L_{SN}(r) = L_{SN} \cdot \frac{e^{-(r/R)^2}}{(R\sqrt{\pi})^3} \ , \tag{3.12}$$

such that 63% of the total luminosity L_{SN} of one SN explosion is injected inside a spherical region of radius R. The mass injection is introduced in the same way. We set $R = 8$ pc.

Since we do not consider radiative cooling, the adiabatic expansion of the gas leads to a process of reducing heat by decreasing the gas pressure (this so-called adiabatic cooling is the only essential energy transformation of our model, which actually transforms internal energy into mechanical energy).

3.3 Numerical methodology

To evolve in space and time the model with initial conditions described in the previous sections, we used a modified version of the numerical MHD code GODUNOV developed by Grzegorz Kowal (see Kowal, Lazarian e Beresnyak 2007, Falceta-Gonçalves, Lazarian e Kowal 2008, Santos-Lima et al. 2010), which uses the Harten-Lax-van-Leer C (HLLC) Riemann solver and a second order Runge-Kutta (Melioli and de Gouveia Dal Pino, 2015) for time integration of the ideal MHD equations (Kadowaki, 2011) of continuity (Eq. 3.13), energy conservation (which in the simplest adiabatic case has the form of Eq. 3.14), momentum (Eq. 3.15) and magnetic induction (Eq. 3.16):

$$\frac{\partial \rho}{\partial t} + \nabla \cdot (\rho \mathbf{v}) = 0 \ , \tag{3.13}$$

$$\frac{\partial u}{\partial t} + \nabla \cdot \left[\left(u + p + \frac{\mathbf{B} \cdot \mathbf{B}}{8\pi} \right) \mathbf{v} - \frac{(\mathbf{v} \cdot \mathbf{B})\mathbf{B}}{4\pi} \right] = \rho \mathbf{g} \cdot \mathbf{v} \ , \tag{3.14}$$

$$\frac{\partial \rho \mathbf{v}}{\partial t} + \nabla \cdot \left[\rho \mathbf{v}\mathbf{v} + \left(p + \frac{\mathbf{B} \cdot \mathbf{B}}{8\pi} \right) \mathbf{I} - \frac{\mathbf{B}\mathbf{B}}{4\pi} \right] = \rho \mathbf{g} \ , \tag{3.15}$$

$$\frac{\partial \mathbf{B}}{\partial t} = \nabla \times (\mathbf{v} \times \mathbf{B}) \ , \tag{3.16}$$

where ρ is the density, $\mathbf{B}$ is the magnetic field which satisfies the condition $\nabla \cdot \mathbf{B} = 0$, p is the thermal pressure, $\mathbf{v}$ is the velocity field, $\mathbf{g}$ is the gravitational field, u is the total energy density of the gas, and $\mathbf{I}$ is the identity tensor.

The code also includes a cooling function for an optically thin gas in ionization equilibrium, and considers the metallicity and the fraction of molecular hydrogen (H_2) of the gas, following the methodology presented in Sobral et al. (2000) and Raga et al. (2002). This radiative cooling is calculated implicitly as a correction to the adiabatic energy conservation equation. In the current simulations, we did not consider this radiative cooling term, which will be introduced in forthcoming tests.

Each simulation was run on 64 processors of the computer cluster of my advisor's group, GAPAE, at IAG-USP.

3.4 Results

Figures 3.3 and 3.4 show the results of the simulated model above the disk after $4.5 \cdot 10^5$ yr, with a resolution of 256^3.

We see in Figure 3.3 an environment whose morphology is nearly compatible with the observations of M82 (see Figure 1.1), with filamentary structures immersed in a wind, which is driven mainly by the Type II SNe exploded in the central 600 pc of the system. The wind reaches a maximum vertical velocity of ~ 190 km/s in the outer shell, therefore the Mach number of $M = 190/30 \sim 6.3$ indicates that it moves supersonically through the disk. We recognize the formation of warm to hot ($\leq 10^7$ K) and dense ($\sim 1 - 10\,\mathrm{cm}^{-3}$) filaments surrounded by a hotter and less dense ISM with temperatures between $\sim 3 \cdot 10^7$ K up to $3 \cdot 10^8$ K and as dense as $0.1\,\mathrm{cm}^{-3}$. The pressure in the central region of starburst activity is of $10^{-3} - 10^{-1}\,\mathrm{dyn/cm}^2$. The ISM was carried away by the SNe shock front and hence we observe a rarefied, warm and low-pressure region ($\leq 10^{-4}\,\mathrm{dyn/cm}^2$) enclosed by a hot and strongly compressed gas with a pressure $\sim 10^{-4} - 10^{-3}\,\mathrm{dyn/cm}^2$.

In Figure 3.4 we observe a typical magnetic field $\sim 10^{-3}\,\mu$G in the low-density gas, of the order of $1\,\mu$G in the compressed interstellar medium, and up to tens of microgauss in the central regions of the galaxy, as observed in the starburst galaxy.

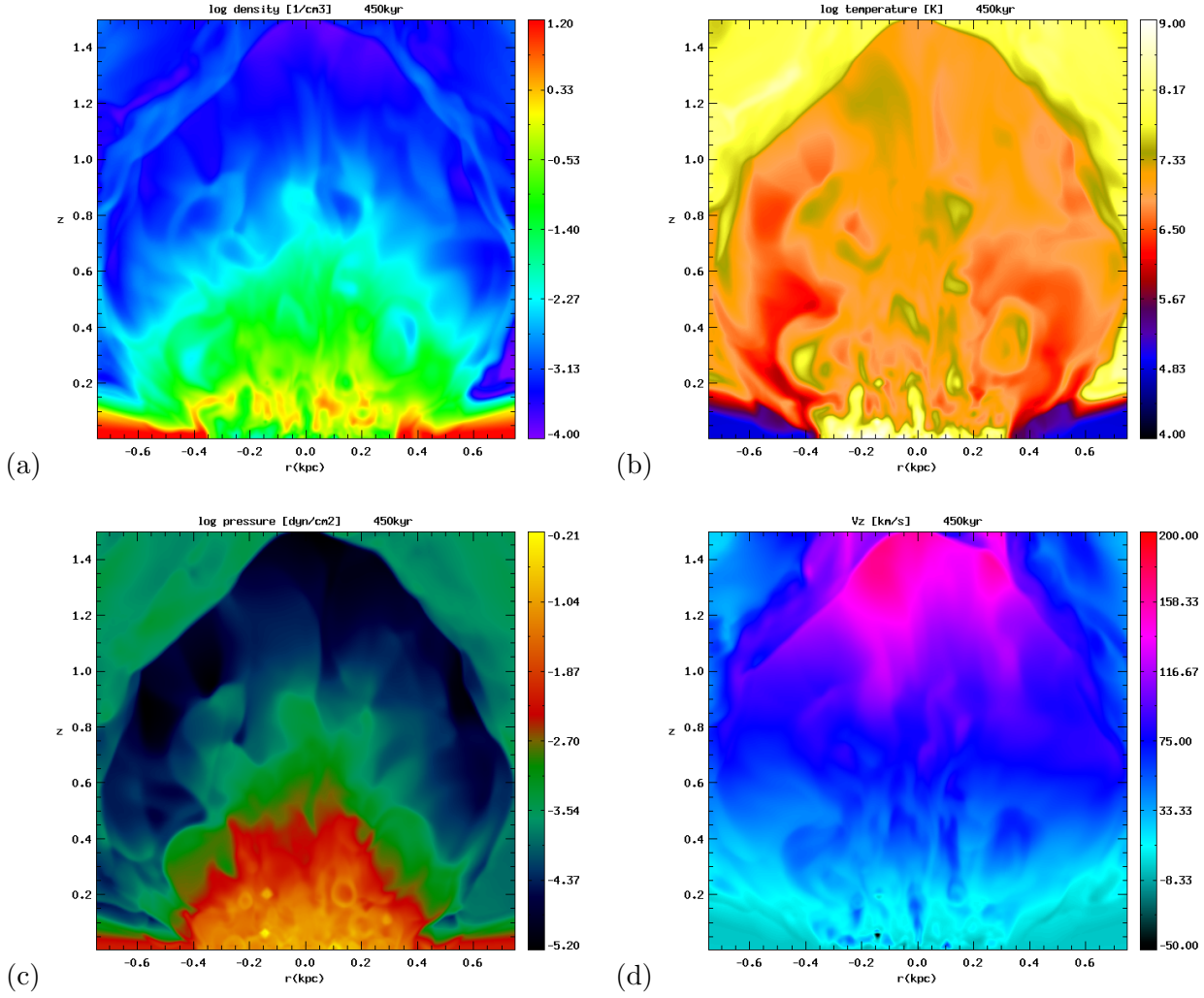

Figure 3.3: Edge-on view of the system at $4.5 \cdot 10^5$ yr. Logarithmic **a**) density, **b**) temperature and **c**) pressure distributions. **d**) Distribution of the velocity in the z-direction. Density is given in cm^{-3}, temperature in Kelvin, pressure in $\mathrm{dyn/cm}^2$, and velocity in km/s. Distances are given in kpc.

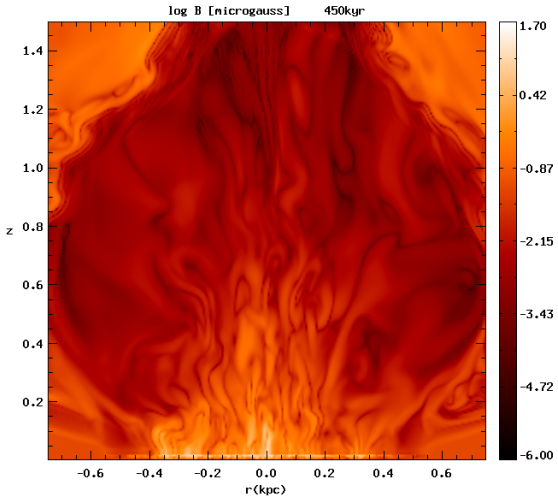

Figure 3.4: Edge-on view of the logarithmic magnetic field distribution after $4.5 \cdot 10^5$ yr. The magnetic field is given in microgauss, distances are in kpc.

3.5 Discussions

The main differences between the system presented in Figure 3.3 and the one that was obtained by Geraissate (2010) and later in Melioli et al. (2013) are due to the presence of radiative cooling of the chemical species in the gas, and are exposed in the temperature, pressure and vertical-velocity distributions. In addition to the system simulated by Geraissate (2010), shown in Figure 3.5, having evolved for $5 \cdot 10^6$ yr, making the filamentary structure to grow and the wind to expand to larger scales than in the case of the present study, the cooling led to a much more complex multi-phase environment, and part of the mechanical energy of the wind was radiated away, giving rise to a colder gas with pressures between 10^{-13} and 10^{-8} dyn/cm^2. Geraissate (2010) also found cold filaments (temperature $\sim 10^4$ K) with lengths of $300 - 1000$ pc, velocities $\sim 200 - 500$ km/s and densities $\sim 10^{-2} - 10\,\mathrm{cm}^{-3}$, similar to what is observed in M82. Besides, the system simulated in their work reproduces quite well the typical pressures and temperatures that are measured from observations of this galaxy. The agreement of the physical conditions reached by Geraissate (2010) with the observations of M82 reveals the importance of taking into account the radiative losses.

According to the conservation equations determined by the Rankine-Hugoniot relations (e.g. Apostila de Plasmas, de Gouveia Dal Pino 2022, Chapter 4), the gas temperature and pressure in adiabatic shocks may raise with the second power of the Mach number, while the density in the shocked regions increases just by a factor 4. This explains why the density distributions we obtained in our adiabatic simulations are comparable to those of Geraissate (2010), while our pressure can be up to eight orders of magnitude larger, as we see in Figure 3.3c.

Of course, we can not neglect the influence of a longer evolution of the system on such differences between the study depicted above and the one performed in Geraissate (2010): the wind, while expanding, leads to the development of cooled, thin and low-pressure phases in the gas.

Finally, side by side with the purely hydrodynamic approach of Geraissate (2010) which did not take the magnetic field effects into consideration, it must be pointed out that the presence of the magnetic field in the current simulations has no major dynamical importance, compared to thermal pressure support, due to the large value of the β parameter.

In the next steps of this work, we will incorporate the effects of the radiative cooling which are already implemented in the code (Melioli and de Gouveia Dal Pino, 2015).

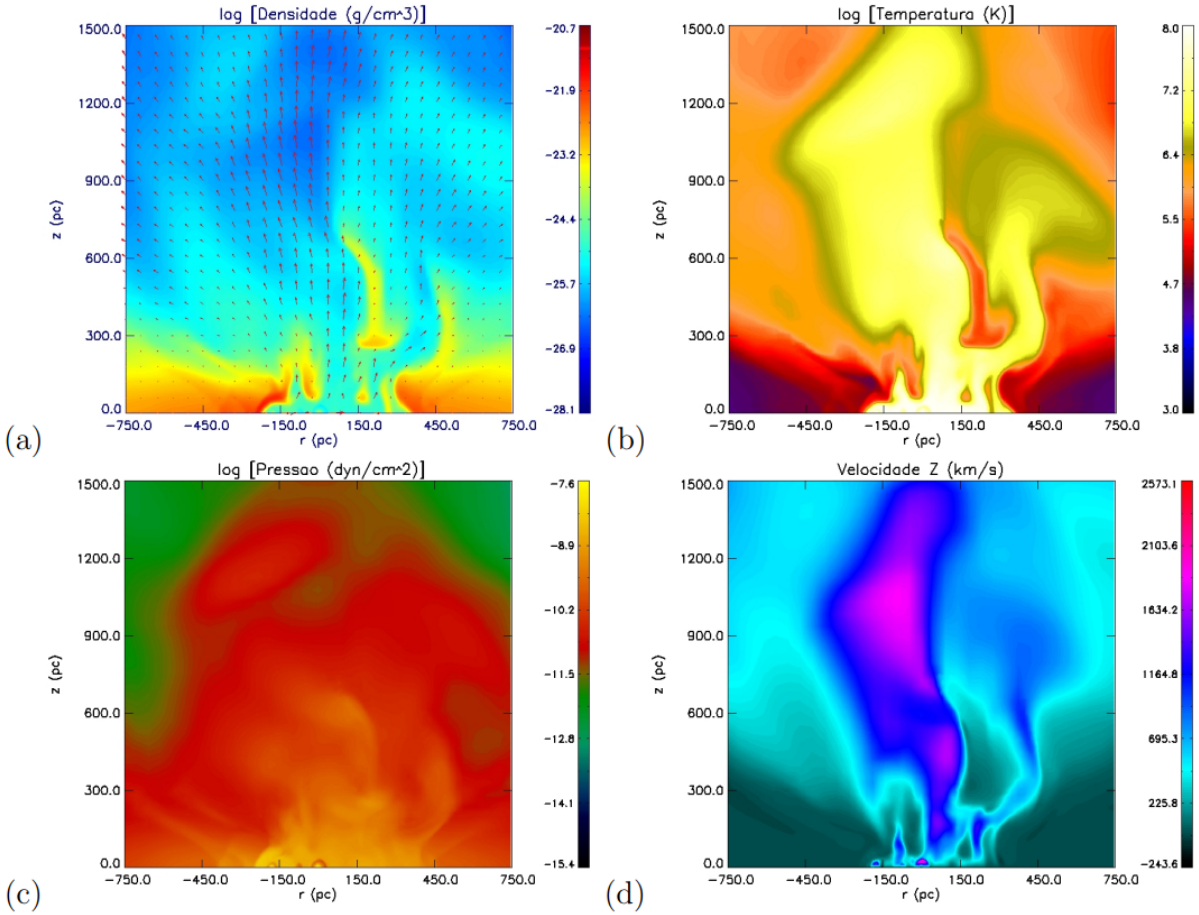

Figure 3.5: Edge-on view of the logarithmic **a**) mass density in g/cm^3, **b**) temperature in Kelvin, **c**) pressure in dyn/cm^2 and **d**) velocity (absolute value) in km/s, of the intermittent wind with radiative cooling after $5 \cdot 10^6$ yr. Distances are given in pc.

Chapter 4

Conclusions and Perspectives

In this study we investigated the implementation of suitable initial conditions for the three-dimensional MHD simulation of the temporal and spatial evolution of galaxies undergoing an exceptionally high rate of star formation, focusing on modeling M82, a prototype of these starburst-like galaxies.

In Chapter 2 we presented the prior stages of the student's graduation work, where we produced predictions of what CTA will observe from three nearby starburst galaxies (M82, NGC253 & Arp220), when operating. We obtained that in a time interval of 100 hours, CTA can be effectively used to resolve the spectral energy distribution of the systems in the very high energies, and that it may provide the first observations of an ULIRG (Arp220) in this band. We employed the reconstructed gamma-ray spectra in order to constrain the CR protons spectral index α and the maximum energy E_{max} of the accelerated hadronic CRs, and we found that the α parameter apparently trends to values ~ 2.3, and that protons reach energies ≥ 500 TeV in both M82 and NGC253, and ≥ 100 TeV in the ULIRG Arp220. CTA observations may also probe whether the galactic wind takes part or not in the high energy emission.

The results of the adiabatic MHD simulations we performed were shown in Chapter 3. We detected a wind (driven mainly by the Type II SNe exploded at a rate $\sim 0.1\,\mathrm{yr}^{-1}$ in the disk within a radius of 300 pc and a height of 160 pc above and below the disk) whose large scale morphological features are nearly compatible to the complex distribution of gas with different densities, pressures, and temperatures that is observed in M82: a warm to hot and dense filamentary structure embedded in a hotter and less dense gas. However, despite having observed a density distribution in agreement with what we foresee for M82 ($\sim 1 - 10\,\mathrm{cm}^{-3}$ in the dense filaments and $\sim 10^{-4} - 10^{-1}\,\mathrm{cm}^{-3}$ in the less dense phases),

we obtained, in the absence of the atomic and molecular radiative cooling of the chemical species of the gas, higher temperatures ($\sim 10^5 - 10^9$ K) and accordingly greater pressures ($\sim 10^{-5} - 1\,\mathrm{dyn/cm^2}$) than what is measured from the observations of this galaxy (Chevalier e Clegg 1985; Tenorio-Tagle e Muñoz-Tuñón 1998; Strickland e Stevens 2000; Tenorio-Tagle, Silich e Munoz-Tunón 2003; Rodriguez-Gonzalez et al. 2008; Cooper, Bicknell, Sutherland e Bland-Hawthorn 2008; Strickland e Heckman 2009) and obtained in previous simulations (Geraissate, 2010; Melioli and de Gouveia Dal Pino, 2015). Additionally, the terminal velocity ~ 190 km/s of the hot "bubble-like" wind perpendicularly to the disk is much smaller than the expected supersonic speed of $\sim 1000 - 2240$ km/s, as well as the filaments velocity of tens of km/s we computed against the observed ~ 600 km/s, but this may be due to the short time of our simulation which probes only the early stages of the wind development. We also noticed that the presence of an initial horizontal magnetic field in the simulation had no major dynamical importance, compared to the thermal pressure support, due to the large value of β parameter we chose ($\beta = 300$).

Although the magnetic fields in M82 are not well known yet, observations of several star-forming galaxies reveal shell-shaped magnetic fields which seem to be coupled with the outflowing gas (Soida et al. 2001, 2002; Soida 2005; Soida et al. 2006), as it can be seen in the outer shell of the wind in Figure 3.4. This coupling may have an essential influence on the acceleration and orientation of the wind (see, e.g., de Gouveia Dal Pino e Medina-Tanco 1999), and could also play a role in the formation of the wind shock front and the filamentary structures, since the presence of the magnetic fields in the shell would make it more difficult to compress the shocked ISM.

In forthcoming work, we intend to account for the effects of radiative cooling which are crucial for a realistic description of the star formation and SN feedback in these systems and in the galactic wind. In the simulation depicted in Chapter 3, the cooling of the gas is due to adiabatic expansion. The presence of radiative cooling will allow for the formation of a much more complex multi-phase environment with much colder and smaller pressure structures and clouds permeated by hot gas, and for part of the mechanical energy of the wind to be radiated away. We will also test other values of the β parameter. Finally, this is an intermediate resolution simulation intended for initial testing, but a simulation performed with a resolution twice as large (see Appendix A) already indicates a good convergence of the results obtained here, at least in the adiabatic regime.

As for the generation of the "simulated data" of starburst galaxies as they will be observed by CTA in the future, we will start employing the Gammapy (Deil et al., 2017), an open-source Python package for gamma-ray analysis built on Numpy and Astropy, in order to produce the predictions of CTA observations, since it has been chosen to be the official Science Analysis Tool library for the CTA Observatory; we may even replicate the work presented in Chapter 2, now making use of Gammapy instead of ctools. For the purpose of adopting our results from the numerical simulations of starburst galaxies as templates for CTA Softwares, we will investigate means of implementing the CRs effects into the simulated environment. In particular, we could employ the CRPropa (Batista et al., 2016), a simulation framework to study the propagation of high energy CRs through an (extra)galactic environment, to propagate CRs through the system we obtain from the MHD simulations in order to reproduce their energy losses by non-thermal processes and to derive the spectral energy distribution of this system in the gamma-ray band.

Bibliography

Abdalla H., Aharonian F., Benkhali F. A., Angüner E., Arakawa M., Arcaro C., Armand C., Arrieta M., Backes M., Barnard M., et al., The starburst galaxy NGC 253 revisited by HESS and Fermi-LAT, A&A, 2018, 617, A73

Abramowski A., Acero F., Aharonian F., Akhperjanian A., Anton G., Balzer A., Barnacka A., Becherini Y., Becker J., Bernlöhr K., et al., Spectral analysis and interpretation of the γ-ray emission from the starburst galaxy NGC 253, ApJ, 2012, 757, 158

Aharonian F., Akhperjanian A., Bazer-Bachi A., Beilicke M., Benbow W., Berge D., Bernlöhr K., Boisson C., Bolz O., Borrel V., et al., A search for very high energy γ-ray emission from the starburst galaxy NGC 253 with HESS, A&A, 2005, 442, 177

Albert J., Aliu E., Anderhub H., Antoranz P., Armada A., Baixeras C., Barrio J., Bartko H., Bastieri D., Becker J., et al., First bounds on the very high energy γ-ray emission from ARP 220, ApJ, 2007, 658, 245

Barker S., De Grijs R., Cerviño M., Star cluster versus field star formation in the nucleus of the prototype starburst galaxy M 82, A&A, 2008, 484, 711

Batista R. A., Dundovic A., Erdmann M., Kampert K.-H., Kuempel D., Müller G., Sigl G., van Vliet A., Walz D., Winchen T., CRPropa 3—a public astrophysical simulation framework for propagating extraterrestrial ultra-high energy particles, JCAP, 2016, 2016, 038

Cherenkov Telescope Array Consortium Science with the Cherenkov Telescope Array, 2019, p. 138, 190

Chevalier R., Clegg A. W., Wind from a starburst galaxy nucleus, Nature, 1985, 317, 44

Cooper J. L., Bicknell G. V., Sutherland R. S., Bland-Hawthorn J., Three-dimensional simulations of a starburst-driven galactic wind, ApJ, 2008, 674, 157

Dalcanton J. J., Williams B. F., Seth A. C., Dolphin A., Holtzman J., Rosema K., Skillman E. D., Cole A., Girardi L., Gogarten S. M., et al., The ACS nearby galaxy survey treasury, ApJS, 2009, 183, 67

de Gouveia Dal Pino E. M., Plasmas em Astrofísica - Curso de Pós Graduação em Astrofísica, 2022

de Gouveia Dal Pino E. M., Medina-Tanco G. A., Magnetically driven outflows in a starburst environment, ApJ, 1999, 518, 129

Deil C., Zanin R., Lefaucheur J., Boisson C., Khelifi B., Terrier R., Wood M., et al., Gammapy - A prototype for the CTA science tools. In 35th International Cosmic Ray Conference (ICRC2017) , vol. 301 of International Cosmic Ray Conference, 2017, p. 766

Engelbracht C., Rieke M. J., Rieke G. H., Kelly D., Achtermann J., The Nuclear starburst in NGC 253, ApJ, 1998, 505, 639

Everett J. E., Zweibel E. G., The Interaction of Cosmic Rays with Diffuse Clouds, ApJ, 2011, 739, 60

Falceta-Gonçalves D., Lazarian A., Kowal G., Studies of regular and random magnetic fields in the ISM: statistics of polarization vectors and the Chandrasekhar-Fermi technique, ApJ, 2008, 679, 537

Ferrara A., McKee C., Heiles C., Shapiro P., The Physics of the Interstellar Medium and Intergalactic Medium. In ASP Conf Series , vol. 80, 1995

Fleischhack H., VERITAS Collaboration Upper limits on the VHE γ-ray flux from the ULIRG Arp 220 and other galaxies with VERITAS. In 34th International Cosmic Ray Conference , 2015, p. 745

Gao Y., Solomon P. M., The star formation rate and dense molecular gas in galaxies, ApJ, 2004, 606, 271

Geraissate F. G., Simulações numéricas hidrodinâmicas tridimensionais de ventos galácticos: uma aplicação à galáxia de Starburst M82, Universidade de São Paulo, 2010, Master Dissertation

Heckman T. M., Armus L., Miley G. K., On the nature and implications of starburst-driven galactic superwinds, ApJS, 1990, 74, 833

Kadowaki L. H. S., Reconexão magnética em discos de acreção e seus efeitos sobre a formação e aceleração de jatos: um estudo teórico-numérico, Universidade de São Paulo, 2011, Ph.D. Thesis

Knödlseder J., Mayer M., Deil C., Buehler R., Bregeon J., Martin P., , 2016 ctools: Cherenkov Telescope Science Analysis Software Astrophysics Source Code Library, record ascl:1601.005

Kowal G., Lazarian A., Beresnyak A., Density fluctuations in MHD turbulence: spectra, intermittency, and topology, ApJ, 2007, 658, 423

Mac Low M.-M., Klessen R. S., Control of star formation by supersonic turbulence, Reviews of Modern Physics, 2004, 76, 125

Mao S. A., Ostriker E. C., Galactic disk winds driven by cosmic ray pressure, ApJ, 2018, 854, 89

Mayya Y., Carrasco L., Luna A., The discovery of spiral arms in the starburst galaxy M82, ApJ, 2005, 628, L33

Melioli C., de Gouveia Dal Pino E. M., Evolution of the ISM of starburst galaxies: The SN heating efficiency, A&A, 2004, 424, 817

Melioli C., de Gouveia Dal Pino E. M., Gas Outflows in Seyfert Galaxies: Effects of Star Formation versus AGN Feedback, ApJ, 2015, 812, 90

Melioli C., de Gouveia Dal Pino E. M., Geraissate F., Evolution of M82-like starburst winds revisited: 3D radiative cooling hydrodynamical simulations, MNRAS, 2013, 430, 3235

Melo V., García A. P., Acosta-Pulido J., Muñoz-Tuñón C., Espinosa J. R., The spatial distribution of the far-infrared emission in NGC 253, ApJ, 2002, 574, 709

Miyamoto M., Nagai R., Three-dimensional models for the distribution of mass in galaxies, PASJ, 1975, 27, 533

O'connell R., Mangano J., The central regions of M82, ApJ, 1978, 221, 62

Pavlidou V., Fields B. D., The guaranteed gamma-ray background, ApJ, 2002, 575, L5

Peretti E., Blasi P., Aharonian F., Morlino G., Cosmic ray transport and radiative processes in nuclei of starburst galaxies, MNRAS, 2019, 487, 168

Peretti E., Morlino G., Blasi P., Cristofari P., Particle acceleration and multimessenger emission from starburst-driven galactic winds, MNRAS, 2022, 511, 1336

Raga de Gouveia Dal Pino, E. M. Noriega-Crespo, A. Mininni, P. D. Velázquez, P. F. Jet/cloud collision, 3D gasdynamic simulations of HH 110, A&A, 2002, 392, 267

Rodriguez-Gonzalez A., Esquivel A., Velázquez P., Raga A., Melo V., Filaments in galactic winds driven by young stellar clusters, ApJ, 2008, 689, 153

Sakamoto K., Mao R.-Q., Matsushita S., Peck A. B., Sawada T., Wiedner M. C., Star-forming cloud complexes in the central molecular zone of NGC 253, ApJ, 2011, 735, 19

Sanders D., Mirabel I., Luminous infrared galaxies, Annual Review of Astronomy and Astrophysics, 1996, 34, 749

Santos-Lima R., Lazarian A., de Gouveia Dal Pino E. M., Cho J., Diffusion of magnetic field and removal of magnetic flux from clouds via turbulent reconnection, ApJ, 2010, 714, 442

Semenov V. A., Kravtsov A. V., Caprioli D., Cosmic-Ray Diffusion Suppression in Star-forming Regions Inhibits Clump Formation in Gas-rich Galaxies, ApJ, 2021, 910, 126

Smith H. E., Lonsdale C. J., Lonsdale C. J., The starburst-AGN connection. II. The nature of luminous infrared galaxies as revealed by VLBI, VLA, infrared, and optical observations, ApJ, 1998, 492, 137

Sobral H., Villagrán-Muniz M., Navarro-González R., Raga A. C., Temporal evolution of the shock wave and hot core air in laser induced plasma, Applied Physics Letters, 2000, 77, 3158

Soida M., Can we observe the poloidal magnetic field?. In The Magnetized Plasma in Galaxy Evolution , 2005, p. 185

Soida M., Beck R., Urbanik M., Braine J., Magnetic fields in the absence of spiral density waves–NGC 4414, A&A, 2002, 394, 47

Soida M., Otmianowska-Mazur K., Chyży K., Vollmer B., Magnetic field evolution in the perturbed Virgo spiral NGC 4654–MHD 3D modeling, Astronomische Nachrichten: Astronomical Notes, 2006, 327, 503

Soida M., Urbanik M., Beck R., Wielebinski R., Balkowski C., Unusual magnetic fields in the interacting spiral NGC 3627, A&A, 2001, 378, 40

Strickland D. K., Heckman T. M., Supernova feedback efficiency and mass loading in the starburst and galactic superwind exemplar M82, ApJ, 2009, 697, 2030

Strickland D. K., Stevens I. R., Starburst-driven galactic winds—I. Energetics and intrinsic X-ray emission, MNRAS, 2000, 314, 511

Tenorio-Tagle G., Muñoz-Tuñón C., The biconical kiloparsec structure generated by nuclear starbursts, MNRAS, 1998, 293, 299

Tenorio-Tagle G., Silich S., Munoz-Tunón C., Supergalactic winds driven by multiple super-star clusters, ApJ, 2003, 597, 279

Appendix

Appendix A

High Resolution Simulations

We have already implemented simulations of the model described before with a maximum resolution of 3.9 pc per cell of a simulated box with physical dimensions of $2 \times 2 \times 2$ kpc covered by 512^3 cells. The results for the system after 375 kyr are shown in Figure A.1.

We found that the results are very similar to those with a 5.8 pc resolution per cell, which indicates a convergence of the results already in this lower resolution. For this reason, although it is undeniable that the high-resolution results are more accurate and attractive, we adopted the lower resolution for the study presented here as it allowed us to save computation time without losing information.

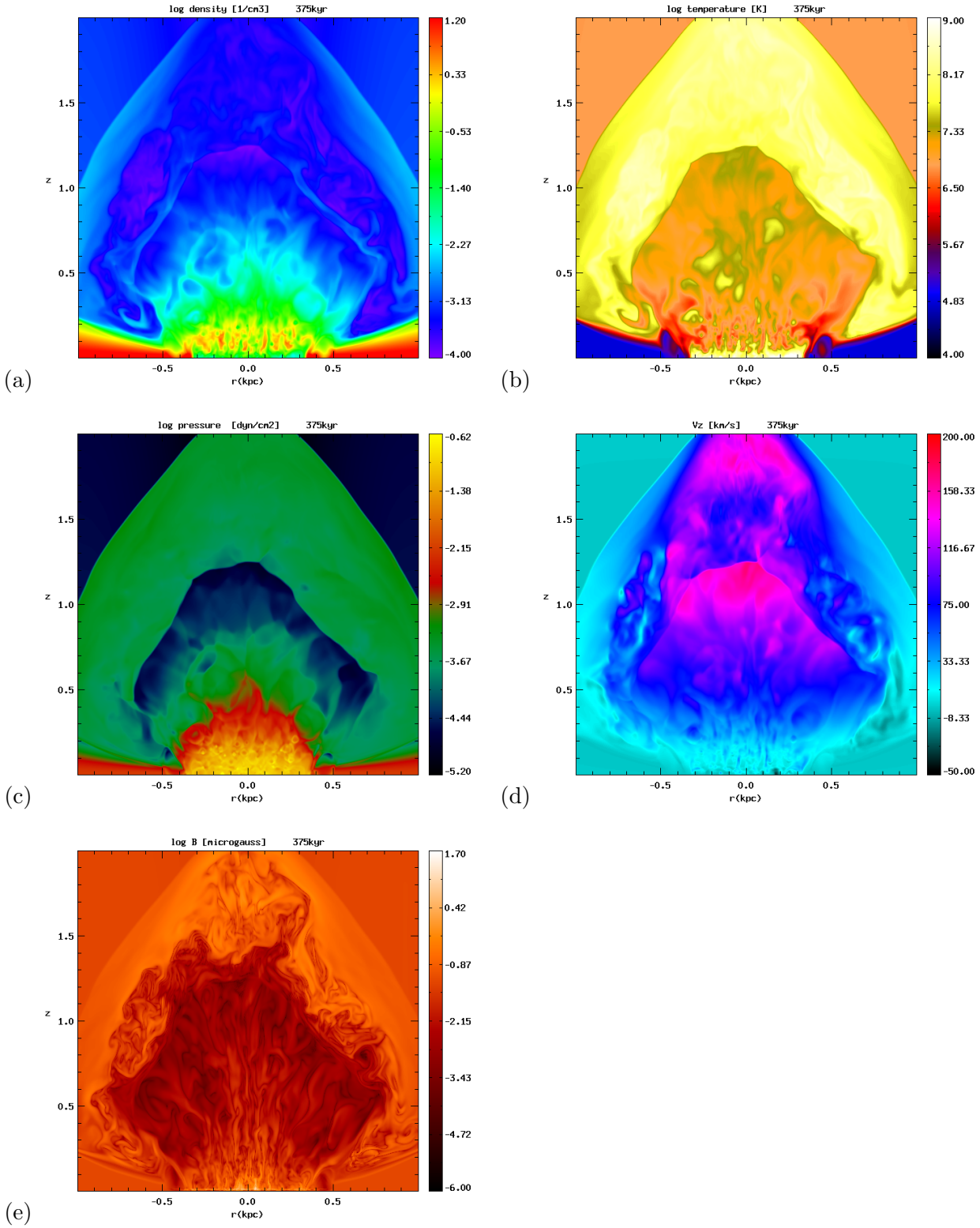

Figure A.1: Edge-on view of the system at $3.75 \cdot 10^5$ yr. Logarithmic **a**) density, **b**) temperature, **c**) pressure and **e**) magnetic field distributions. **d**) Distribution of the velocity in the z-direction. Density is given in cm^{-3}, temperature in Kelvin, pressure in $\mathrm{dyn/cm}^2$, velocity in km/s, and magnetic field in microgauss. Distances are given in kpc. The resolution is 512^3